Identification of the most relevant metal impurities in mc *n*-type silicon for solar cells

J. Schön [a,*], F. Schindler [a,b], W. Kwapil [a,b], M. Knörlein [a], P. Krenckel [a], S. Riepe [a], W. Warta [a], M.C. Schubert [a]

[a] *Fraunhofer Institute for Solar Energy Systems, Heidenhofstr. 2, 79110 Freiburg, Germany*
[b] *Freiburger Materialforschungszentrum FMF, Albert-Ludwigs-Universität Freiburg, Stefan-Meier-Str. 21, 79104 Freiburg, Germany*

ABSTRACT

In general, the charge carrier lifetime in *n*-type silicon is less sensitive to common dissolved metals compared *to p*-type silicon. However, in experiments it was observed that metal impurities limit the lifetime in *n*-type multicrystalline (mc) silicon even if high purity feedstock was used. By evaluating Neutron Activation Analysis (NAA) and Inducitvely Coupled Plasma Mass Spectrometry (ICP-MS) at blocks grown with high purity feedstock, we identified the main currently unavoidable metal impurities present in *n*-type mc silicon. In addition, we measured the charge carrier lifetime on surface-passivated wafers after different solar cell processes. The measurements were compared to simulations in order to identify the limitations by different impurities and to evaluate the influence of metal precipitates. We found that Cr_i is an important defect in good grains of as-grown wafers. Dissolved Co can have a severe impact on lifetime after process steps with fast cooling. The lower lifetime in the edge region of the blocks is attributed to $FeSi_2$ precipitates, which explains the poor gettering response of the edge region in contrast to grains in the block center. From the results obtained for $FeSi_2$-precipitates, we concluded that Cu_3Si- and $NiSi_2$-precipitates located at crystal defects may be responsible for significant recombination in the block center.

1. Introduction

Solar cell production from *n*-type mc silicon is potentially an interesting alternative to conventional routes due to the relatively low crystallization costs if the high efficiency potential can be realized that is expected from the tolerance against common metal impurities [1]. While new crystallization methods are able to reduce the density of harmful crystal defects [2–4], an impurity contamination from the crucible system cannot be fully avoided during crystallization at present.

The charge carrier lifetime in *n*-type mc silicon can be improved during phosphorus diffusion [5,6], which is a clear indication for limitation by metallic impurities. Furthermore, the charge carrier lifetime is reduced in the edge and top regions of *n*-type blocks [5,6], where the impurity concentration is higher due to solid state diffusion. Vähänissi et al. [6] found that the lifetime gain resulting from a low temperature anneal at the end of the phosphorus diffusion decreases towards the block edge. They attributed this behavior to the increasing concentration of

precipitated impurities. Although it is of common agreement that interstitial Fe plays only a minor role in *n*-type silicon, a significantly reduced charge carrier lifetime in intentionally Fe contaminated *n*-type mc silicon was found by Coletti et al. [7], indicating that Fe might not be as harmless as expected. The reasons might be sought in the presence of $FeSi_2$-precipitates: in Ref. [8] the injection-dependent lifetime in the edge region of a *p*-type block is explained by a combination of dissolved and precipitated Fe. From an analysis of the Shockley–Read–Hall recombination parameters, Schmidt et al. [9] identified Cr, Co and Ni as harmful metallic impurities. However, up to now, no experimental result has been published clarifying the impact of different impurities on carrier lifetime limitations in pure *n*-type mc silicon.

This work aims to close the knowledge gap by evaluating the limitation of the charge carrier lifetime in *n*-type Si before and after solar cell processes. For *the n*-type crystals, manufactured in a laboratory-type crystallization furnace, high purity feedstock and clean standard industrial quality crucibles were used to evaluate the challenges of *n*-type mc silicon for high efficiency solar cells. Hence, we dispose of the full information about temperature gradients and about the impurity concentrations in the feedstock and the crucible system. We analyzed the impurity concentrations at several blocks to identify the metal impurities in significant

---

concentrations which are then analyzed in detail. The detailed study includes Co and Cr which are assumed to play an important role in *n*-type mc silicon [9], dissolved and precipitated Fe, the most prominent impurity in *p*-type mc silicon, as well as Cu₃Si- and NiSi₂-precipitates. We simulated the impurity distribution after crystallization and after phosphorus diffusion, yielding the precipitate size distributions, and the recombination of charge carriers at FeSi₂-precipitates using the models on which the analysis of the injection-dependent lifetime in the edge region of a *p*-type block is based [8]. In addition, we measure the injection-dependent charge carrier lifetime at several positions of an *n*-type block of size G2. Metastable defect imaging of interstitial Fe and Cr distributions in an mc Si *p*-type "sister" block (identical crystallization process, furnace, crucible, and feedstock; differing only in the type of doping) gives access to their concentrations also in *the n*-type block.

2. Experiment

Two mc-Si blocks of size G2 (width 40 cm; height 22.5 cm) were crystallized from high purity feedstock under the same conditions; the blocks differing only by their doping type, i.e. boron or phosphorus. Clean standard crucibles were used for the crystallization. The resistivity in the *n*-type block decreases from 3.5 Ω cm at the bottom to 0.7 Ω cm close to the top. Another *n*-type block of size G1 (width 22 cm; height 12.8 cm) was overcompensated by adding boron in the Si melt during the crystallization process, i.e. after solidification of ∼25% of the Si. This block delivers *n*- and *p*-type "sister" wafers with very similar impurity concentrations and virtually identical crystal structure. The overcompensated block allows analyses without unavoidable uncertainties that arise in a comparison of two blocks, like the exact thickness of the edge cut before wafering or small temperature variations.

The uncertainties of impurity measurements by NAA or ICP-MS are rather high (see e.g. [10]) and the detection limits for metals vary significantly. Thus, we evaluated NAA and ICP-MS data from several blocks. The samples were cut from horizontal slices at 50% block height. Neutron activation analyses (NAA) were performed at the two G2 blocks and with lower detection limits for most metals at G1 *p*-type block ("NAA block") crystallized in 34 h (instead of 50 h for the G2) with a coating that has slightly different metal concentrations, e.g. $[Cr]=4.0\times10^{16}$ cm⁻³ ("NAA block") instead of 5.7×10^{16} cm⁻³ (G2).The concentrations of the important metals in the crucible are compared to the concentrations measured by ICP-MS in Ref. [11]. For coating the same clean standard powder was used as in Ref. [11].

Parallel wafers from different block heights of the G2 blocks were divided into two groups: "as-grown" and "P-Diff". After seeing damage etching the wafers from the "P-Diff" group underwent a POCl₃–N₂ diffusion process at 800 °C. Afterwards, the phosphorus-doped layer was etched off. The wafers from both groups were surface-passivated with a SiN layer deposited at 250 °C (*n*-type) or with an Al₂O₃-layer deposited at 200 °C (*p*-type) prior to an anneal at 400 °C (*n*- and *p*-type).

The injection-dependent charge carrier lifetime measured was spatially resolved by photoluminescence (PL) imaging. The PL images were lifetime-calibrated by harmonically modulated photoluminescence measurements [12,13]. The local interstitial Fe (Fe_i) and interstitial Cr (Cr_i) distributions in *p*-type wafers were determined by measuring the charge carrier lifetime in the interstitial and the boron-paired state at a generation level corresponding to 1/100 suns [14–17]. We assume similar precipitation kinetics for Fe and Cr in *p*- and *n*-type silicon, which is justified for higher temperatures at which the Fermi-level effect is negligible.

Then, the fraction of the total charge carrier recombination due to Fe_i and Cr_i in *n*-type silicon was calculated from the charge carrier lifetime in *the n*-type wafer and using the SRH-defect parameters for *n*- and *p*-type Si [17,18], assuming that the Fe_i or Cr_i distributions in the *p*-type Si wafer from the same block position are valid for *the n*-type Si wafer. Here, the injection dependence of Fe_i and Cr_i in *n*- and *p*-type Si was taken into account. After the crystallization process the Fe_i and Cr_i concentrations are lower at crystal defects. Since the exact positions of these crystal defects cannot be considered in the calculation the fraction of charge carrier recombination due to Fe_i and Cr_i at these crystal defects is slightly overestimated.

3. Simulations

3.1. Diffusion and precipitation during solidification and high-temperature steps

3.1.1. Iron

We used the models described in Ref. [19] for the simulation of Fe precipitation. However, the model structure was modified: the enhanced nucleation site density is now restricted to an area of only 20×20 nm² around one dislocation line. The reproduction of former precipitate size distributions [19,20] and Fe_i concentrations required a recalibration of the model parameters due to the smaller areas with high nucleation site density. For the presented simulations, we used a nucleation site line density along dislocations of 2.5×10^5 cm⁻¹. In the precipitation model, an effective local solubility [21] and radius [22] depending on the size of precipitates are used for the calculation of the dissolution and growth rates of FeSi₂ precipitates with the Fokker–Planck equation [20]. For small FeSi₂ precipitates, the flux of dissolved iron atoms to the precipitates is determined by the effective radius of the nucleation sites [20], which is $r_{SD}=20$ nm in our model. The precipitate radius depends on the Fe atoms in the precipitate N_{Fe} by $r_{prec}=(r_{SD}^3+8\times10^{-24}\times N_{Fe})^{1/3}$. Grain boundaries are treated as a two-dimensional assembly of dislocation lines. For the simulations of the FeSi₂ precipitate distribution in good grains, we assumed a dislocation density of 3.3×10^3 cm⁻².

The model for in-diffusion of Fe from the crucible and coating into the liquid and solidified silicon is described in Ref. [10]. In combination with the modified Scheil equation and the precipitation model, it allows the prediction of the Fe distribution in the Si crystal-crucible system [10,23]. The emitter formation was simulated with the phosphorus diffusion model from Ref. [24]. The model for phosphorus diffusion gettering is based on the effect of segregation of dissolved Fe into the emitter, due to an increased solubility in highly phosphorus-doped silicon [25,26]. We used the segregation coefficient depending on the active phosphorus concentration from Ref. [27].

3.1.2. Chromium

For the simulation of the Cr distribution in the Si crystal-crucible system, the same in-diffusion model as for Fe and Co [10] was used. It was shown in Ref. [28] that the Fe precipitation model including the model parameters can be used for reproducing the Cr precipitation processes, using the diffusivity [29] and solubility [30] for Cr. However, the diffusivity inside the crucible and the coating as well as the segregation coefficient between the crucible system and solidified silicon had to be determined. The comparison between simulations and measurements and the found parameters are presented in Appendix A.

3.1.3. Cobalt

We simulated the in-diffusion of Co from the crucible and the coating into the liquid and solidified silicon with the model and parameters presented in Ref. [10]. Substitutional Co is the dominating state of dissolved Co in silicon at room temperature and quite detrimental in *n*-type silicon [9,31]. However, Co has a high diffusivity, a low solubility in relation to the diffusivity and precipitates homogeneously [31]. Thus Co is mainly precipitated in slowly cooled samples. An exact calibration of the Co precipitation model was not possible with the existing data for Co precipitation in mc silicon. However, we can estimate the maximum fraction of the detrimental dissolved Co by applying the model for heterogeneous Fe precipitation [10] using the diffusivity and solubility of Co [30]. The additional homogeneous precipitation mechanism for Co leads to a further reduction of the dissolved Co concentration. The solubility of Co at 800 °C (i.e. phosphorus diffusion temperature) is almost 10^{13} cm^{-3}. Thus, in equilibrium Co is completely dissolved inside the wafers during phosphorus diffusion. Co is at least as effectively gettered as Fe [32], i.e. the concentration decreases by around two orders of magnitude for the applied process.

3.2. Model for charge carrier recombination at precipitates

The injection dependent charge carrier recombination at metal precipitates was simulated with a two-dimensional model assuming a radial symmetry around the dislocations at which the precipitates are placed. The model and parameters for charge carrier recombination at metal precipitates are taken from Ref. [8]. In the model the interface between silicon and FeSi$_2$ precipitates is described as a Schottky contact leading to the formation of a space charge region around the precipitates. The size distribution of FeSi$_2$ precipitates along a dislocation is taken from the simulation described in Section 3.1. The recombination due to Cu$_3$Si and NiSi$_2$ precipitates is calculated with the parametrization of Ref. [33].

4. Limitation of the charge carrier lifetime

In Fig. 1 the charge carrier lifetime of parallel *n*-type wafers from 19% block height at a generation rate of 0.05 suns before (a) and after (b) phosphorus diffusion are shown. Phosphorus diffusion is not included in many *n*-type solar cell process sequences. However, it gives a good hint at the nature of the dominant defects and the potential of the material as the highest charge carrier lifetimes are measured after phosphorus diffusion

[5]. The dominant defect in as-grown grains is getterable and mobile at 800 °C which results in a strong increase of the lifetime during phosphorus diffusion. The weaker gettering efficacy in the edge region and the dislocation clusters indicate that less mobile or additional not getterable defects are present. The contribution of the different dissolved and precipitated impurities is studied in the following sections.

4.1. Selected dissolved impurities in n-type Si

4.1.1. Cobalt

4.1.1.1. After crystallization. Co is assumed to play an important role in mc *n*-type silicon [9] because substitutional Co, the dominating state of dissolved Co at room temperature, is quite detrimental in *n*-type silicon due to the high capture cross section for holes [9,31]. If we assume that Co is mainly dissolved, the Co concentrations measured by NAA (Fig. 2(a)) would result in a strong lifetime limitation throughout the whole block. Furthermore, the lifetime due to Co would increase by more than one order of magnitude between a distance of 50 mm from the crucible and 120 mm from the crucible which is not observed in the lifetime measurement. The absence of a correlation between the measured lifetime (black dots in Fig. 2(b)) and the total Co concentration can be explained by the high diffusivity of Co and a resulting fast precipitation. The precipitation of Co is further intensified by the solubility of Co which is the lowest of the fast diffusing transition metals and the ability of homogeneous precipitation in silicon.

We estimate the maximum remaining fraction of dissolved Co after the crystallization process with simulations of the Co indiffusion and precipitation (Fig. 2(a)). The total Co concentrations measured at samples from various edge distances and heights of the G2 block are well predicted by the simulations within the uncertainties of NAA. The simulation predicts a dissolved Co concentration after crystallization of only $\sim 5 \times 10^8$ cm^{-3} which is almost independent of the distance from crucible (Fig. 2(a), black solid line). A calculation of the Shockley–Read–Hall lifetime using the parameters from Refs. [31,34] reveals that the simulated lifetime due to dissolved Co is almost two orders of magnitude above the measured lifetime (Fig. 2(b)) and thus can be neglected.

4.1.1.2. After phosphorus diffusion. During phosphorus diffusion Co dissolves and is gettered into the heavily doped surface regions. The total Co concentration decreases by around two orders of magnitude for the applied process. Nevertheless, the predicted concentrations of dissolved Co are higher after phosphorus
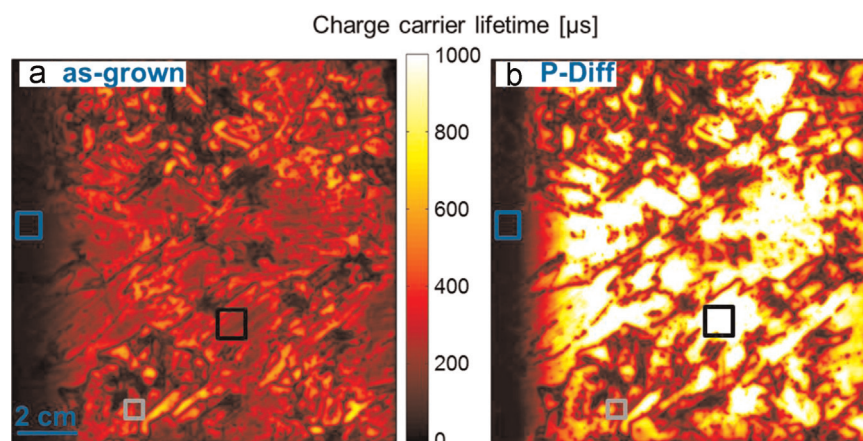

Fig. 1. Charge carrier lifetime of an *n*-type wafer before (a) and after (b) phosphorus diffusion at 19% block height at a generation rate of 0.05 suns. The injection dependent lifetime in the color marked rectangles are shown in Figs. 6–8. (For interpretation of the references to color in this figure, the reader is referred to the web version of this article.)
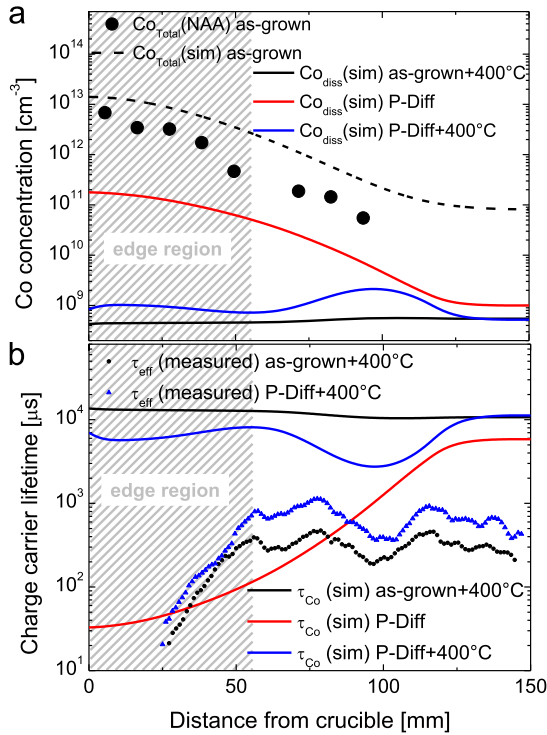
Fig. 2. (a) Measured (NAA) and simulated total Co profiles for the G2 block (50% block height). In addition simulations of dissolved Co concentrations after crystallization and after phosphorus diffusion with and without subsequent 400 °C annealing are plotted. (b) Comparison of the measured lifetime (averaged PL linescan) and the lifetime due to simulated dissolved Co (shown in (a)) after different process steps. No correlation between the lifetime limitations due to the simulated dissolved Co concentrations and the measured lifetimes is observed. The lifetime decrease at a distance of around 100 mm is due to a large dislocation cluster (see Fig. 1). (For interpretation of the references to color in this figure, the reader is referred to the web version of this article.)

diffusion then after crystallization due to the faster cooling ramps (red line in Fig. 2(a)). In the simulation Co is mainly dissolved directly after phosphorus diffusion. From the simulation we can estimate the limited lifetime due to dissolved Co to 6 ms in the center and below 100 μs in the edge region. According to this simulation, dissolved Co is an important impurity directly after phosphorus diffusion for distances less than 110 mm from the crucible and only of minor importance in the block center.

Unfortunately, we are not able to prove this finding experimentally. The charge carrier lifetime in Fig. 2(b) was measured after SiN passivation (annealed at 250 °C for 20 min followed by 10 min at 400 °C). The annealing step leads to precipitation of Co and thus a reduction of the dissolved Co concentration by more than one order of magnitude according to the simulations (blue line in Fig. 2(a)). This finding is confirmed by the measurements at processed wafers: the measured mean bulk lifetime is higher than expected from the simulations without 400 °C annealing and does not decrease between a distance of 50 and 110 mm from the edge [5] (Fig. 2(b)), at which the total Co concentration increases significantly. The simulated bulk lifetime after phosphorus diffusion and 400 °C annealing is again significantly higher than the measured lifetime. We can conclude that Co might get severe depending on the applied high temperature step, even if the analyzed lifetime samples are not influenced by Co.

4.1.2. Chromium

Under the likely assumption that the diffusion and precipitation of Cr is similar in p- and n-type Si, the fraction of charge carrier recombination due to Cr_i in n-type wafers can be determined. Fig. 3(c) shows this fraction in an n-type wafer from 45%

block height at a generation rate of 0.05 suns using the measured charge carrier lifetime in *the n*-type wafer (Fig. 3(a)) and the averaged Cr_i concentration measured in the p-type wafer of the same block height (see Fig. 3(b)). Due to the low lifetime level and the resulting high detection limit for Cr_i in the edge region of the p-type wafer, we are not able to measure the Cr_i concentration in this region. Thus, we extrapolate the Cr_i measurements according to our simulation results for the edge region (see Figs. 10 and 3(b)).

From our analysis we conclude that Cr_i is responsible for 20–60% of the recombination in good grains of as-grown n-type wafers. In the low lifetime areas, i.e. the areas with high dislocation density, Cr_i is of minor importance. The fraction of recombination due to Cr_i is not increased in the edge region. Thus, other impurities are dominating the lifetime in the edge region.

To verify these finding and quantify the fraction of recombination due to Cr_i in dependence of the injection level, we compare in Fig. 4 the injection dependent lifetime due to Cr_i with the measured injection dependent lifetime in the good grain marked with a green rectangle in Fig. 3(a). Due to the decreasing Cr_i related lifetime for increasing injection level, Cr_i dominates the lifetime around an injection level of 10^{15} cm^{-3}. As a result, the lifetime due to Cr_i and Auger recombination matches the measured lifetime for high injection levels within the measurement uncertainty of the Cr_i concentration ($[Cr_i] = 1.2 \pm 0.5 \times 10^{10}$ cm^{-3}). An additional defect is necessary to describe the measured lifetime in the low injection regime.

After high temperature steps and especially phosphorus diffusion we expect a strong decrease in the Cr_i concentration and thus a reduced influence of Cr_i on the charge carrier lifetime [28].

4.1.3. Iron

For Fe_i a similar evaluation as for Cr_i is performed (Fig. 3(d)): the measured spatially resolved lifetime in the same n-type edge wafer is compared with the Fe_i-limited SRH-lifetime for n-type silicon obtained from the Fe_i measurement in the corresponding p-type wafer with respect to the wafer edge (see Section 2). The used averaged Fe_i linescan obtained from the Fe_i imaging on the p-type wafer can be seen in Fig. 3(b). Although the mean fraction of charge carrier recombination due to Fe_i is quite low, Fe_i should be considered in good grains with high Fe concentration, e.g. the edge or top regions of blocks. The influence of Fe_i on the charge carrier lifetime is known to be strongly reduced after phosphorus diffusion gettering [19].

4.2. Lifetime limitation in the edge region

The edge region, which is caused by impurities diffused into the solidified block from the crucible-coating system, is almost as wide for *the n*-type as for the p-type block grown under similar conditions (bottom graph of Fig. 5(a)). Thus, lifetime in the edge region of *the n*-type block is either limited by (i) an in-diffused impurity with a slightly lower diffusivity than Fe or (ii) a Fe correlated defect that starts to dominate at higher Fe concentrations compared to Fe_i in p-type.

From all metal impurities found with chemical methods, the diffusivity of Mn, besides Cr, (see analysis in Section 4.1 and Appendix A), is comparable to Fe at high temperatures and thus can be a candidate for the lifetime limitation in the edge. The charge carrier recombination due to Mn_i calculated from the SRH parameters from Refs. [36,37] is approximately five times higher in n-type silicon than the recombination at the same amount of Fe_i. However, a Mn concentration of 4.4×10^{12} cm^{-3} (slightly above the ICP-MS detection limit) was measured close to the crucible in the block analyzed in Ref. [11], which is more than two orders of magnitude lower than the Fe concentrations. Furthermore, we expect much lower Mn concentrations throughout the whole

block due to the relatively low Mn concentrations in the crucible and the coating [11]. As an example we estimate the dissolved Mn concentration and the resulting lifetime limitation in a grain from the edge region (blue rectangle in Fig. 1(a)) to 2×10^{11} cm^{-3}, respective 1.3 ms. Thus, even if Mn is completely dissolved it could not be a dominant impurity in the edge region with charge carrier lifetimes below 100 μs.

Metallic FeSi$_2$ precipitates are the most likely candidates for Fe correlated defects, due to the high concentrations of precipitated Fe in the edge region [10]. Since there is no experimental method to directly detect their distribution on a macroscopic scale, as indirect evidence for their influence the simulated profiles of precipitated Fe and Fe$_i$ are presented in Fig. 5(a) together with the Fe$_i$ measurements at the p-type block (top). The concentration profiles are compared to the lifetime profiles close to the edge (bottom) in both, the p- and n-type Si block. The decrease of lifetime towards the edge in the p-type Si-block correlates with an increase of the Fe$_i$ concentration, whereas the decrease of lifetime in the analyzed n-type wafers correlates with the increase of precipitated Fe.

We confirmed the slightly smaller edge region in n-type compared to p-type at the transition region of an overcompensated block (Fig. 5(b)). Also, the higher lifetime level in n-type Si is visible in the lower part of the image. As in Fig. 5(a), the low lifetime region in n-type Si is slightly smaller compared to the p-type Si. Without the overcompensation, the edge region would decrease with increasing block height.

4.2.1. FeSi$_2$ precipitates after crystallization

In a next step, we measured the injection dependent lifetime in an edge grain of the wafer from 19% block height (blue rectangle in Fig. 1(a)), which is plotted in Fig. 6(a). In this grain we expect a total Fe concentration of around 4×10^{13} cm^{-3} from the simulations. The measured lifetime is compared to the simulated charge carrier lifetime due to FeSi$_2$ precipitates for the simulated precipitate size distribution in the edge grain (Fig. 6). In the edge region at least as much other defects are present as in a center grain without a significant lifetime limitation by Fe. Thus, we add the recombination in a center grain (black rectangle in Fig. 1(a),
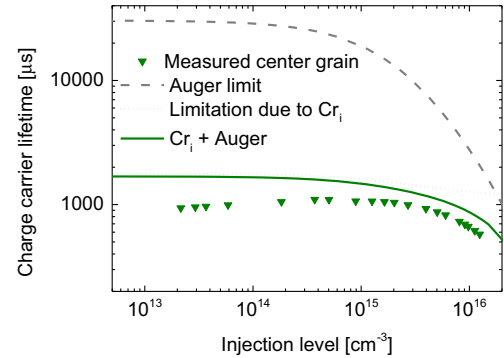

Fig. 4. Measured injection dependent lifetime in a grain from center region (green triangles: green rectangle in Fig. 3(a)). The measured injection dependence is close to the expected curve from the measured Cr$_i$ concentration in the p-type wafer from the sister block (green line). (For interpretation of the references to color in this figure legend, the reader is referred to the web version of this article.)
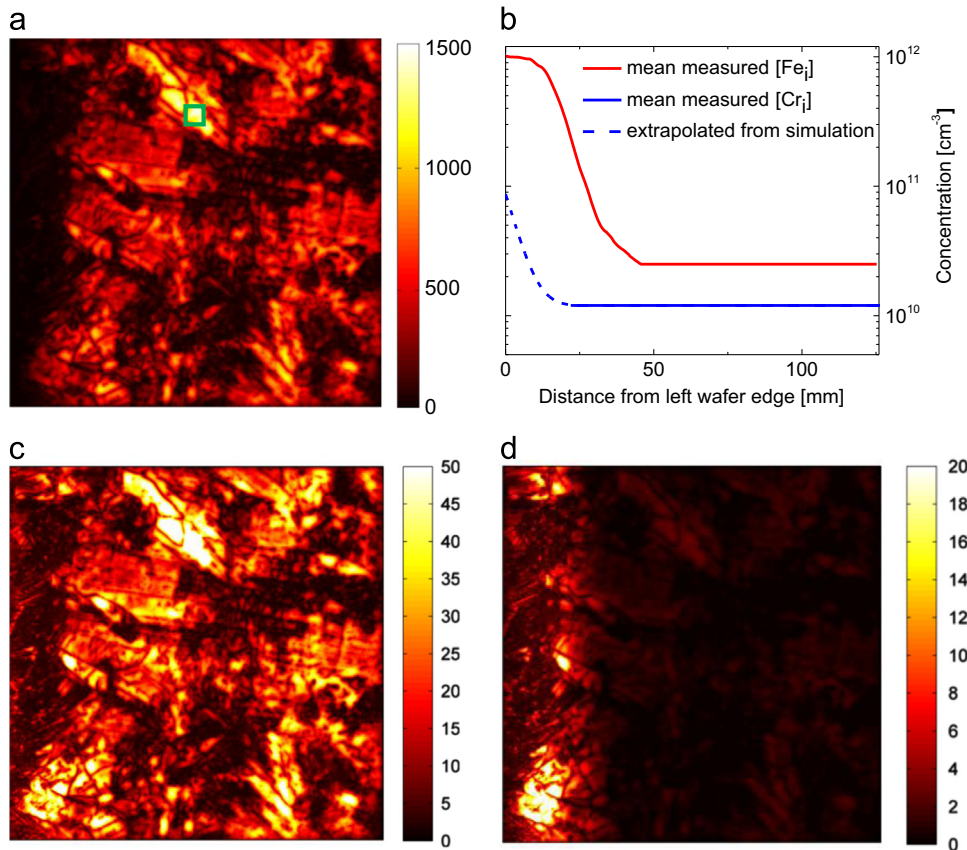

Fig. 3. (a) Charge carrier lifetime measurement of an n-type wafer (12.5 × 12.5 cm²) from 45% block height illuminated by 0.05 suns (block edge on the right side). The fraction of charge carrier recombination due to Cr$_i$ and Fe$_i$ is shown in (c) and (d). Note the different scale of (c) and (d). The Cr$_i$ and Fe$_i$ profiles used for the calculation of (c) and (d) are extracted from a p-type wafer of the same block height and shown in (b). (For interpretation of the references to color in this figure, the reader is referred to the web version of this article.)
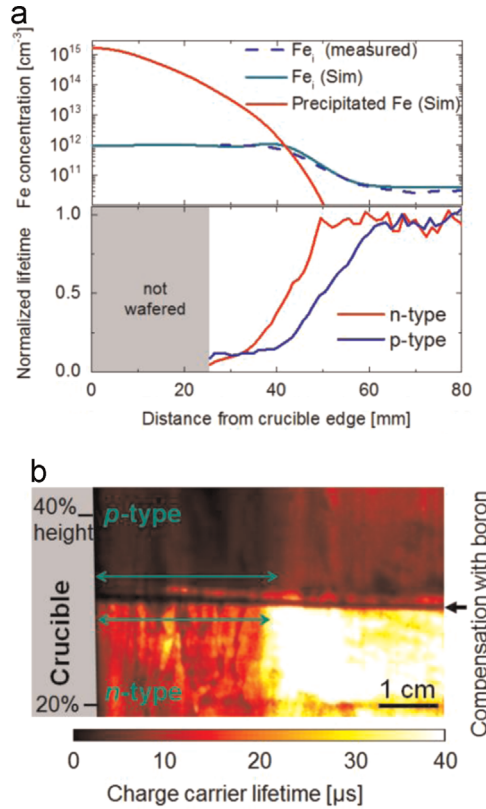
Fig. 5. (a) Top: simulated profiles of precipitated Fe and Fe_i together with the Fe_i profile measured at the p-type block at 19% block height. Bottom: measured lifetime in n- and p-type wafers from the same block height (n-type wafer from Fig. 1 (a)). (b) PL based lifetime measurement [13,38] at a vertical slice at the transition region of an overcompensated block, taking the varying doping concentration into account. The edge region with lower lifetime is visible in n- and p-type Si. The transition from n- to p -type doping comes along with a small area of low net doping which results in an artificially low lifetime in the PL lifetime image (dark horizontal line).

black diamonds in Fig. 6) to the recombination related to $FeSi_2$ precipitates and Fe_i (simulation: 1.1×10^{12} cm^{-3}). Furthermore, the increased Cr_i concentration (simulation: 2.8×10^{10} cm^{-3}) and Mn concentration (estimation: 2×10^{11} cm^{-3}) in the edge are taken into account. The resulting theoretical injection dependent lifetime (solid blue line in Fig. 6) is already close to the measured lifetime curve in the edge grain. An exact reproduction of the measured lifetime in the edge cannot be expected. The concentrations of all other metals increase towards the edge which results in additional recombination channels, e.g. as SRH defects, precipitates or decorated dislocations. The measured injection dependence has a slighter slope than the simulated curve indicating that the lifetime of the additional defects increases only slightly with injection level.

4.2.2. $FeSi_2$ precipitates after phosphorus diffusion

Precipitated Fe is less effectively gettered than most dissolved impurities due to the incomplete dissolution during phosphorus diffusion. For an analysis of the limitation due to $FeSi_2$ precipitates after the phosphorus diffusion process, we simulate simultaneously phosphorus diffusion, gettering and precipitate dissolution. The predicted injection dependent lifetime due to $FeSi_2$ precipitates after phosphorus diffusion is shown in Fig. 7(a). Besides the initial Fe concentration of 4×10^{13} cm^{-3} expected for the measured grain in the edge, we show the results for four times higher initial Fe concentrations. Higher initial Fe concentration
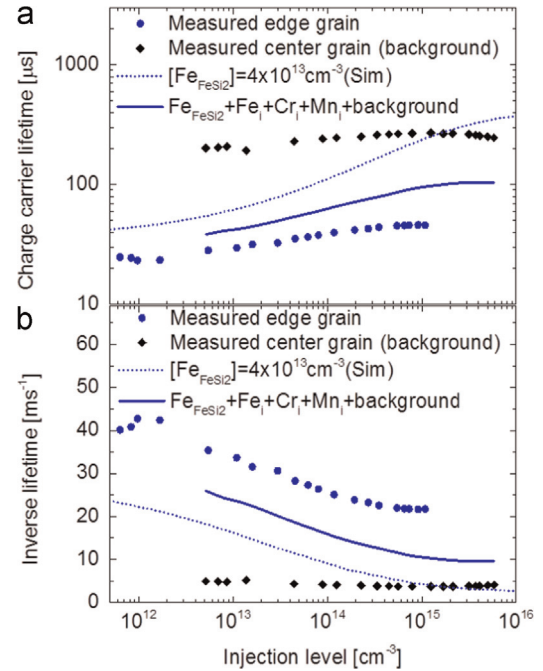

Fig. 6. (a) Measured injection dependent lifetime in a grain from center region (black diamonds: black rectangle in Fig. 1(a))) and edge region (blue circles: blue rectangle in Fig. 1(a)) as well as the simulated lifetime due to $FeSi_2$ precipitates in the edge region. (b) The sum of the measured inverse lifetime in the center grain and the simulated inverse lifetime due to $FeSi_2$ precipitates, enhanced Fe_i, Cr_i and Mn_i concentrations in the edge region explains the major part of the measured inverse lifetime in the edge grain. (For interpretation of the references to color in this figure legend, the reader is referred to the web version of this article.)

results in larger precipitates that have a smaller injection dependency [8].

The lifetime limitation due to the $FeSi_2$ precipitates for an initial Fe concentration of 4×10^{13} cm^{-3} is compared with the measured charge carrier lifetime in an edge grain after phosphorus diffusion (blue squares: blue rectangle in Fig. 1(b)), taking the background lifetime measured in a center grain (black stars: black rectangle in Fig. 1(b)) and the Fe_i concentration into account (Fig. 7). Both, the measured charge carrier lifetime in the edge grain as well as the simulated lifetime due to $FeSi_2$ precipitates increase only slightly during phosphorus diffusion (see Fig. 6 for comparison). It should be noted that the gettering efficacy of precipitated Fe depends strongly on the temperature of the applied phosphorus diffusion process.

The comparison of the measured and simulated inverse lifetime (Fig. 7(b)) demonstrates that a large part of the recombination in the edge grain can be explained by $FeSi_2$ precipitates, especially at low injection levels. However, the differences between the measured inverse lifetime in the edge and the center grain cannot be fully explained by the simulated $FeSi_2$ precipitates. The analyzed edge grain might have a higher density of structural defects compared to the chosen center grain which has a relatively high lifetime compared to surrounding grains (Fig. 1(b)). Another reason might be the uncertainties in the Fe precipitate size distribution which are drastically enhanced due to the uncertainty in the distance of the analyzed grain from the crucible (± 5 mm). Even initial Fe concentrations of up to 1.5×10^{14} cm^{-3} cannot be fully excluded. For the identification of the dominant edge defect the position of the edge region and the consistency of the measured lifetime increase due to phosphorus diffusion and simulated gettering efficacy is thus of utmost importance.
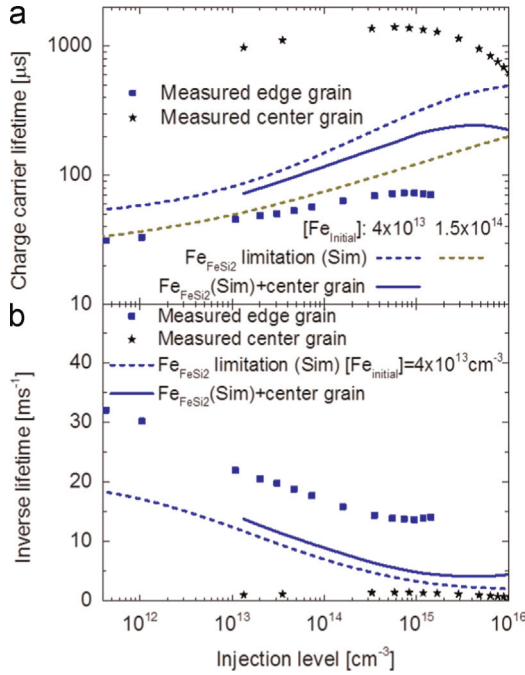
Fig. 7. (a) Measured injection dependent lifetime in a grain from center region (black stars: black rectangle in Fig. 1(b))) and from the edge region (blue squares: blue rectangle in Fig. 1(b)). Additionally, the limitation by $FeSi_2$ precipitates after phosphorus diffusion gettering for an initial Fe concentration of 4×10^{13} cm^{-3} and 1.5×10^{14} cm^{-3} are shown. (b) The sum of the measured inverse lifetime in the center grain region and the simulated inverse lifetime due to $FeSi_2$ precipitates and Fe_i in the edge region ([$Fe_{initial}$]=4×10^{13} cm^{-3}) is between 1/3 and 2/3 below the measured inverse lifetime in the edge grain. (For interpretation of the references to color in this figure legend, the reader is referred to the web version of this article.)

4.3. Other metal impurities

NAA measurements of the "NAA block" and ICP-MS measurements are analyzed to identify other metal impurities that have the potential to limit the charge carrier lifetime. For Ti, which is found in significant concentration in the crucible (1.6×10^{17} cm^{-3}) and the coating (3×10^{16} cm^{-3}), the detection limits of ICP-MS and NAA are too high for an analysis. We would expect a rather homogeneous Ti distribution due to the low diffusivity. However, from the resulting SRH lifetime a homogeneous Ti concentration above 3×10^{10} cm^{-3} at medium block positions can be excluded due to the measured lifetime in good grains and the weak gettering response of Ti. For other metals like W or Mo the measured concentrations are small or below a low detection limit in the analyzed blocks. Even if the measured metal concentrations or the maximum concentrations (in case of detection limits) are assumed to be dissolved, a significant influence of the resulting SRH lifetimes on the measured charge carrier lifetime can be excluded. In the block center of the NAA block a Cu concentration of [Cu]$_{NAA}$=6×10^{13} cm^{-3} is found which is slightly higher than ICP-MS data from Ref. [11] ([Cu]$_{ICP-MS}$=$2-4 \times 10^{13}$ cm^{-3}). Ni concentrations measured by ICP-MS ([Ni]$_{ICP-MS}$=$2-3 \times 10^{13}$ cm^{-3}) [11] are comparable to the Cu concentrations. Both metal concentrations increase slightly towards the block edge ($\sim 1 \times 10^{14}$ cm^{-3}). Dissolved Ni, unlike Cu, is quite hazardous in *n*-type silicon [9]. However, since Ni has a high diffusivity (comparable to Co diffusivity) significant fractions of dissolved Ni can only be achieved in mc Si after fast cooling. The same holds for Cu.

Cu_3Si precipitates can significantly reduce the charge carrier lifetime in mc silicon [39]. Thus, we estimated the recombination due to Cu_3Si and $NiSi_2$ precipitates with the model from Ref. [33]. The Cu concentration in a G2 block varies significantly due to in-diffusion from the crucible [40]. We expect lower metal
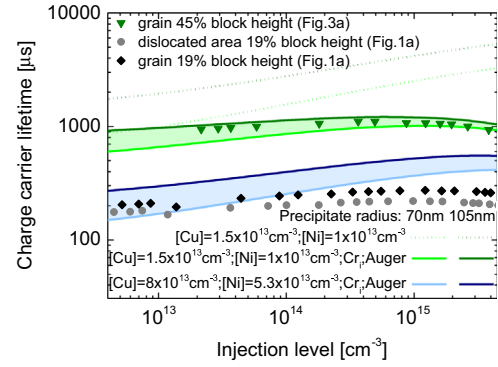

Fig. 8. Estimated charge carrier lifetime limit due to Cu_3Si and $NiSi_2$ precipitates of different sizes and densities. Additional recombination due to Cr_i and Auger is considered in the dotted lines. For comparison the measured injection dependent lifetime for two spots from 19% block height (black and gray rectangles in Fig. 1(a)) and for a spot from 45% block height (green rectangle in Fig. 3(a)) are shown. (For interpretation of the references to color in this figure legend, the reader is referred to the web version of this article.)

concentration for 45% and higher metal concentrations for 19% block height: [Cu]=8×10^{13} cm^{-3} ([Ni]=5.3×10^{13} cm^{-3}) at 19% and [Cu]=1.5×10^{13} cm^{-3} ([Ni]=1×10^{13} cm^{-3}) at 45%. For Cu_3Si and $NiSi_2$ precipitates, we expect a larger mean precipitate size compared to $FeSi_2$ precipitates for the same total impurity concentration due to the higher diffusivity enabling precipitate ripening. The lifetime limitation due to $FeSi_2$ precipitates for a total Fe concentration of 4×10^{13} cm^{-3} (Fig. 6) can be roughly described if all $FeSi_2$ precipitates have a radius between 35 nm and 40 nm, thus giving a lower limit for Cu_3Si and $NiSi_2$ precipitates. In Fig. 8 the injection dependent lifetime limitations due to Cu_3Si and $NiSi_2$ precipitates with a radius of 70 and 105 nm are plotted for the expected Ni and Cu concentrations in the center of the G2 block at 45% block height. The simulated influence on the lifetime is larger for $NiSi_2$ precipitates compared to Cu_3Si precipitates due to the larger precipitate volume per metal atom. In addition, the measured injection dependent lifetimes in few grains from 19% and 45% block height are plotted for comparison with the simulated lifetime due to Cu_3Si and $NiSi_2$ precipitates, Cr_i and Auger recombination.

For both block positions the simulated lifetime due to precipitates, Cr_i and Auger is only slightly above, or in the case of a radius of 70 nm at 45% block height slightly below, the measured lifetime. Additionally, the measured injection dependence is fairly well reproduced.

The uncertainties in the lifetime simulation due to the unknown radius of the precipitate become obvious by comparing the results for 70 nm with 105 nm in Fig. 8. As expected, the lifetime due to precipitates increases and the injection dependence decreases with increasing radius. In reality a distribution of precipitates of different size is expected, which can influence the height and the shape of the injection dependent lifetime. We expect a mean radius closer to 70 nm for 45% block height and a mean radius closer to 105 nm for 19% block height due to the corresponding Cu and Ni concentration. Furthermore, we expect laterally inhomogeneous concentrations on the mm scale due to the high diffusion length of Cu and Ni during the cooling down after crystallization. This might be an explanation for the underestimated lifetime for the small grain from 45% block height for a (more likely) average radius of 70 nm, i.e. some of the Cu and Ni from the grain diffused towards the grain boundaries during the crystallization process.

Both, Cu_3Si and $NiSi_2$ precipitates are completely dissolved during high temperature processing and can be effectively gettered by phosphorus diffusion [41]. Due to the high uncertainties
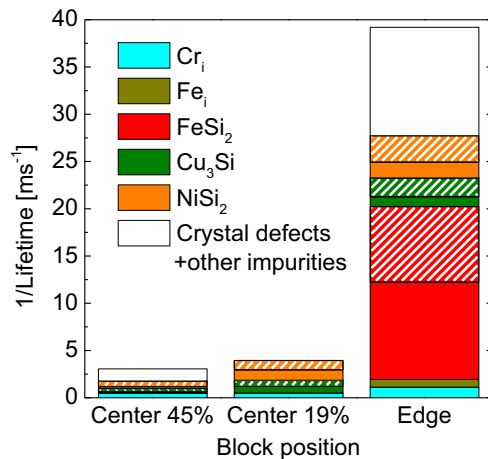
Fig. 9. Fraction of inverse lifetime due to the different defects in three block regions. Note that the lifetime is taken from the whole center/edge regions of the wafers including dislocation clusters and not only from the grains analyzed in Section 4. The hatched bars indicate the uncertainties of the precipitate simulations and might be part of the lifetime limitation due to the corresponding precipitates or assigned to "crystal defects+other impurities".

Fig. 10. Simulated and measured Cr concentration for two different blocks. The three NAA measurement points at distances between 8 and 32 mm were below the shown detection limit. The NAA value at the sample ∼55 mm away from the crucible is close to the detection limit, has high uncertainties and is in contradiction to the Cr_i imaging and typical in-diffusion profiles [10]. Thus we neglect this NAA value for the determination of the model parameters.

of the precipitate evolution and gettering of Ni and Cu, we are not able to give a clear conclusion of the lifetime limitation due to Cu_3Si and $NiSi_2$ precipitates after solar cell process. The lifetime of the three measured spots increases during phosphorus diffusion. However, the relative increase of the lifetime differs strongly (injection level of ∼10^{14} cm^{-3}): 400% (black rectangle in Fig. 1(a)), 140% (green rectangle in Fig. 3(a)) and only 30% (gray rectangle in Fig. 1(a)). Thus, either the concentrations of Cu and Ni differ in the analyzed spots or an additional less/not getterable defect is present in the gray rectangle in Fig. 1(a).

In addition to the discussed dissolved and precipitated impurities, dislocations decorated with single impurity atoms influence the charge carrier recombination. An experimental determination of the fraction of charge carrier recombination and the gettering behavior of impurity atoms at dislocations is challenging.

5. Conclusions

We analyzed two G2 blocks crystallized with electronic-grade feedstock and coating and crucible of clean industrial quality, which are the main impurity sources. For larger industrial blocks we expect lower metal concentrations in the center and slightly broader edge regions [10]. The measured edge regions of *n*-type blocks are almost as wide as the edge regions of *p*-type blocks crystallized under the same conditions. Our simulations indicate that mainly $FeSi_2$ precipitates located at crystal defects are responsible for the low lifetime in the edge regions (see Fig. 9). A similar influence of $FeSi_2$ precipitates is expected for the top region of the block.

Cr_i limits the lifetime in good grains and is responsible for more than 50% of the recombination in the best grains of as-grown wafers. The simulations predict a minor influence of $FeSi_2$ precipitates in non-contaminated center regions. However, precipitates of Cu and Ni are responsible for additional recombination. An estimation of the lifetime limitation due to Cu_3Si and $NiSi_2$ precipitates demonstrates that the recombination due to Cu_3Si and $NiSi_2$ precipitates can be associated with the getterable recombination centers in the block center other than Cr_i. We found that Cu_3Si and $NiSi_2$ precipitates dominate in the lower part of block. A significant influence of almost all other dissolved or precipitated metal impurities on the lifetime can be excluded. The
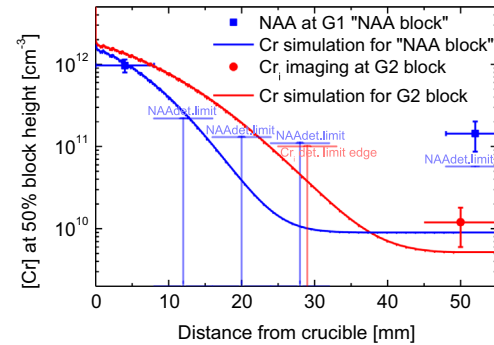
recombination activity of crystal defects can be partly explained by the metal precipitates, which preferentially nucleate at these defects. However, crystal defects decorated with single impurity atoms are also important, especially if large dislocation cluster are present (e.g. in the center wafer from 45% block height). The increased significance of the crystal defects in the edge can be explained by an increased decoration of these defects. After phosphorus diffusion the lifetime in the edge regions increases only slightly due to the less effective gettering of $FeSi_2$ precipitates. In the center regions the lifetime limitation by metals is strongly reduced due to the high gettering efficacy of dissolved Cr and precipitated Cu and Ni. After fast cooling dissolved Co and Ni might get important.

Appendix A

In analogy to Fe and Co in Ref. [10], the Cr diffusivity inside the crucible and the coating as well as the segregation coefficient between the crucible system and solidified silicon were determined. Cr concentrations of 1.6×10^{16} cm^{-3} for the used crucibles and 5.7×10^{16} cm^{-3} ("NAA block": 4.0×10^{16} cm^{-3}) for the coating were found with ICP-MS. The Cr concentration in the feedstock measured by ICP-MS is 1.5×10^{12} cm^{-3}. After crystallization the total Cr concentration was measured by NAA in the "NAA block" and the dissolved Cr concentration by Cr_i imaging in the *p*-type G2 block. Only one of the NAA measurements is well above the detection limit, the other four NAA measurements give only upper bounds (see Fig. 10). Four ICP-MS measurement series (20 measurements in total) performed at mid-block heights samples from blocks crystalized with the same coating as the G2 block were mostly below the detection limit of 1.6×10^{12} cm^{-3}. The three ICP-MS measurements slightly above the detection limit were measured within the first 18 mm, but do not show a clear trend. The (few significant) data points allow only a rough determination of the Cr diffusivity in the crucible

$D_{Crucible}$, in the coating $D_{Coating}$ and the segregation coefficient between coating and solidified silicon k_{Segre} (Coating/Si). The NAA data in the edge region is reproduced by assuming the following parameters in the simulations (see Fig. 10):

$$D_{Crucible} = 50 \times \exp(-3./k_B T)$$

$$D_{Coating} = 3 \times \exp(-3.05/k_B T)$$

$$k_{Segre}(\text{Coating/Si}) = 1.5 \times 10^{-4}$$

The diffusivity of Cr in the crucible has only a small influence on the results and is chosen similar to the Fe diffusivity [10]. For the determination of the Cr concentration in the block center with the modified Scheil equation [10,27], we use a segregation coefficient of 2×10^{-5} between liquid and solidified silicon.

We conclude from former measurements [28] that most of the Cr is dissolved if concentrations are below 10^{12} cm^{-3}. Thus, we suppose that Cr$_i$ imaging gives a good estimate for the total concentration in the block center (see Fig. 10). The Cr$_i$ measurement outside the edge region is in accordance with the simulations and indicates that the NAA measurement at the sample $\sim$55 mm away from the crucible wall is already below the detection limit. Unfortunately, Cr$_i$ imaging at the wafer edge gives only an upper limit for the Cr$_i$ concentration due to the high Fe$_i$ concentrations and the resulting low charge carrier lifetimes in *p*-type silicon.

References

[1] D. Macdonald, L.J. Geerligs, Recombination activity of interstitial iron and other transition metal point defects in p- and n-type crystalline silicon, Appl. Phys. Lett. 85 (2004) 4061–4063.

[2] M. Di Sabatino, G. Stokkan, Defect generation, advanced crystallization, and characterization methods for high-quality solar-cell silicon, Phys. Status Solidi A 210 (2013) 641–648.

[3] X. Tang, L.A. Francis, L. Gong, F. Wang, J.-P. Raskin, D. Flandre, et al., Characterization of high-efficiency multi-crystalline silicon in industrial production, Sol. Energy Mater. Sol. Cells 117 (2013) 225–230.

[4] Y.M. Yang, A. Yu, B. Hsu, W.C. Hsu, A. Yang, C.W. Lan, Development of high-performance multicrystalline silicon for photovoltaic industry, Prog. Photovolt.: Res. Appl. 23 (2015) 340–351.

[5] F. Schindler, B. Michl, A. Kleiber, H. Steinkemper, J. Schon, W. Kwapil, et al., Potential gain in multicrystalline silicon solar cell efficiency by n-type doping, IEEE J. Photovolt. 5 (2015) 499–506.

[6] V. Vähänissi, M. Yli-Koski, A. Haarahiltunen, H. Talvitie, Y. Bao, H. Savin, Significant minority carrier lifetime improvement in red edge zone in n-type multicrystalline silicon, Sol. Energy Mater. Sol. Cells 114 (2013) 54–58.

[7] G. Coletti, R. Kvande, V.D. Mihailetchi, L.J. Geerligs, L. Arnberg, E.J. Øvrelid, Effect of iron in silicon feedstock on p- and n-type multicrystalline silicon solar cells, J. Appl. Phys. 104 (2008) 104913.

[8] W. Kwapil, J. Schon, F. Schindler, W. Warta, M.C. Schubert, Impact of iron precipitates on carrier lifetime in as-grown and phosphorus-gettered multicrystalline silicon wafers in model and experiment, IEEE J. Photovolt. 4 (2014) 791–798.

[9] J. Schmidt, B. Lim, D. Walter, K. Bothe, S. Gatz, T. Dullweber, et al., Impurity-related limitations of next-generation industrial silicon solar cells, IEEE J. Photovolt. 3 (2013) 114–118.

[10] M.C. Schubert, J. Schön, F. Schindler, W. Kwapil, A. Abdollahinia, B. Michl, et al., Impact of impurities from crucible and coating on mc-silicon quality – the example of iron and cobalt, IEEE J. Photovolt. 3 (2013) 1250–1258.

[11] W. Kwapil, A. Zuschlag, I. Reis, I. Schwirtlich, S. Meyer, R. Zierer, et al., Influence of crucible and coating on the contamination of directionally solidified silicon: first results of the German research network "SolarWinS", in: Proceedings of the 27th EUPVSEC, 2012, pp. 627–635.

[12] J.A. Giesecke, M.C. Schubert, B. Michl, F. Schindler, W. Warta, Minority carrier lifetime imaging of silicon wafers calibrated by quasi-steady-state photoluminescence, Sol. Energy Mater. Sol. Cells 95 (2011) 1011–1018.

[13] J.A. Giesecke, M.C. Schubert, F. Schindler, W. Warta, Harmonically modulated luminescence: bridging gaps in carrier lifetime metrology across the PV processing chain, IEEE J. Photovolt. 5 (2015) 313–319.

[14] D. Macdonald, J. Tan, T. Trupke, Imaging interstitial iron concentrations in boron-doped crystalline silicon unsing photoluminescence, J. Appl. Phys. 103 (2008) 73710.

[15] M.C. Schubert, H. Habenicht, W. Warta, Imaging of metastable defects in silicon, IEEE J. Photovolt. 1 (2011) 168–173.

[16] H. Habenicht, M.C. Schubert, W. Warta, Imaging of chromium point defects in p-type silicon, J. Appl. Phys. 108 (2010) 34909.

[17] C. Sun, F.E. Rougieux, D. Macdonald, Reassessment of the recombination parameters of chromium in n- and p-type crystalline silicon and chromium–boron pairs in p-type crystalline silicon, J. Appl. Phys. 115 (2014) 214907.

[18] A.A. Istratov, H. Hieslmair, E.R. Weber, Iron and its complexes in silicon, Appl. Phys. A (Mater. Sci. Process.) 69 (1999) 13–44.

[19] J. Schön, H. Habenicht, M.C. Schubert, W. Warta, Understanding the distribution of iron in multicrystalline silicon after emitter formation: theoretical model and experiments, J. Appl. Phys. 109 (2011) 63717.

[20] A. Haarahiltunen, H. Väinölä, O. Anttila, M. Yli-Koski, J. Sinkkonen, Experimental and theoretical study of heterogeneous iron precipitation in silicon, J. Appl. Phys. 101 (2007) 43507.

[21] M. Aoki, A. Hara, Re-emission of iron originally gettered by oxygen precipitates in a silicon wafer, J. Appl. Phys. 74 (1993) 1440.

[22] A. Haarahiltunen, H. Talvitie, H. Savin, O. Anttila, M. Yli-Koski, M.I. Asghar, et al., Gettering of iron in silicon by boron implantation, J. Mater. Sci.: Mater. Electron. 19 (2008) S41–S45.

[23] B. Mitchell, D. Macdonald, J. Schon, J.W. Weber, H. Wagner, T. Trupke, Imaging as-grown interstitial iron concentration on boron-doped silicon bricks via spectral photoluminescence, IEEE J. Photovolt. 4 (2014) 1185–1196.

[24] J. Schön, A. Abdollahinia, R. Müller, J. Benick, M. Hermle, W. Warta, et al., Predictive simulation of doping processes for silicon solar cells, Energy Procedia 38 (2013) 312–320.

[25] S.M. Myers, M. Seibt, W. Schröter, Mechanisms of transition-metal gettering in silicon, J. Appl. Phys. 88 (2000) 3795–3819.

[26] J. Schön, M.C. Schubert, W. Warta, H. Savin, A. Haarahiltunen, Analysis of simultaneous boron and phosphorus diffusion gettering in silicon, Phys. Status Solidi A 207 (2010) 2589–2592.

[27] B. Michl, J. Schön, W. Warta, M.C. Schubert, The impact of different diffusion temperature profiles on iron concentrations and carrier lifetimes in multicrystalline silicon wafers, IEEE J. Photovolt. 3 (2013) 635–640.

[28] J. Schön, H. Habenicht, W. Warta, M.C. Schubert, Chromium distribution in multicrystalline silicon: comparison of simulations and experiments, Prog. Photovolt.: Res. Appl. 21 (2013) 676–680.

[29] N.T. Bendik, V.S. Garnik, L.S. Milevskii, Precipitation kinetics of solid solutions of chromium in silicon, Sov. Phys. Solid State 12 (1) (1970) 150–154.

[30] E.R. Weber, Transition metals in silicon, Appl. Phys. A (Solids Surf.) 30 (1983) 1–22.

[31] S. Diez, S. Rein, T. Roth, S.W. Glunz, Cobalt related defect levels in silicon analyzed by temperature- and injection-dependent lifetime spectroscopy, J. Appl. Phys. 101 (2007) 33710.

[32] M. Seibt, A. Sattler, C. Rudolf, O. Voß, V. Kveder, W. Schröter, Gettering in silicon photovoltaics: current state and future perspectives, Phys. Status Solidi 203 (2006) 696.

[33] W. Kwapil, J. Schön, W. Warta, M.C. Schubert, Carrier recombination at metallic precipitates in p- and n-type silicon, IEEE J. Photovolt. (2015), accepted.

[34] W. Jost, J. Weber, H. Lemke, Hydrogen-induced defects in cobalt-doped n-type silicon, Semicond. Sci. Technol. 11 (1996) 22–26.

[36] K. Graff, Metal Impurities in Silicon-Device Fabrication, Springer, Berlin, 1999.

[37] P. Rosenits, D. Macdonald, Lifetime studies on manganese implanted silicon, in: Proceedings of the 21st EUPVSEC, Dresden, Germany, 2006, pp. 953–956.

[38] J.A. Giesecke, R.A. Sinton, M.C. Schubert, S. Riepe, W. Warta, Determination of bulk lifetime and surface recombination velocity of silicon ingots from dynamic photoluminescence, IEEE J. Photovolt. 3 (2013) 1311–1318.

[39] J. Lindroos, Y. Boulfrad, M. Yli-Koski, H. Savin, Preventing light-induced degradation in multicrystalline silicon, J. Appl. Phys. 115 (2014) 154902-1–154902-5.

[40] S. Riepe, I.E. Reis, W. Kwapil, M.A. Falkenberg, J. Schön, H. Behnken, et al., Research on efficiency limiting defects and defect engineering in silicon solar cells – results of the German research cluster solarfocus, Phys. Status Solidi C 8 (2010) 733–738.

[41] M.B. Shabani, T. Yamashita, E. Morita, Metallic impurities in mono and multicrystalline silicon and their gettering by phosphorus diffusion, ECS Trans. 16 (6) (2008) 179–193.